Stability Control of Gob-Side Entry Retaining in Fully Mechanized Caving Face Based on a Compatible Deformation Model

Xinshuai Shi[1], Hongwen Jing[1, *], Jianguo Ning[2], Zhenlong Zhao[1] and Junfu Zhu[1]

Abstract: The stability control of gob-side entry retaining in fully mechanized caving face is a typical challenge in many coal mines in China. The rotation and subsidence of the lateral cantilever play a critical role in a coal mine, possibly leading to instability in a coal seam wall or a gob-side wall due to its excessive rotation subsidence. Hence, the presplitting blasting measures in the roof was implemented to cut down the lower main roof and convert it to caved immediate roof strata, which can significantly reduce the rotation space for the lateral cantilever and effectively control its rotation. Firstly, the compatible deformation model was established to investigate the quantitative relationship between the deformation of the coal seam wall and the gob-side wall and the subsidence of the lateral cantilever. Then, the instability judgments for the coal seam wall and gob-side wall were revealed, and the determination method for the optimal roof cutting height were obtained. Furthermore, The Universal Distinct Element Code numerical simulation was adopted to investigate the effect of roof-cutting height on the stability of the retained entry. The numerical simulation results indicated that the deformation of the roadway could be effectively controlled when the roof-cutting height reached to 18 m, which verified the theoretical deduction well. Finally, a field application was performed at the No. 3307 haulage gateway in the Tangan coal mine, Ltd., Shanxi Province, China. The field monitoring results showed that the blasting roof cutting method could effectively control the large deformation of surrounding rocks, which provided helpful references for coal mine safety production under similar conditions.

Keywords: Gob-side entry retaining, fully mechanized caving face, lateral cantilever, compatible deformation model, the optimal roof cutting height.

[1] State Key Laboratory for Geomechanics and Deep Underground Engineering, China University of Mining and Technology, Xuzhou, 221116, China.

[2] College of Mining and Safety Engineering, Shandong University of Science and Technology, Qingdao, 266510, China.

[*] Corresponding Author: Hongwen Jing. Email: hongwenjingcumt@126.com.

Received: 15 July 2019; Accepted: 10 March 2020.

1 Introduction

In recent years, the fully mechanized caving face (FMCF) has been widely implemented in Chinese coal mines [Wang, Ning, Jiang et al. (2018)]. With the improvement of the production capacity of the coalface, the relative gas emission increases significantly [Wang, Yang, Li et al. (2014); Zhang, Bai, Chen et al. (2015); Li, Liu, Dai et al. (2020)]. In particular, for highly gassy coal mines, the gas is quickly accumulated in the upper corner of the mining face in the conventional "U" type longwall mining system (see Fig. 1(a)), possibly causing a gas explosion to occur. Moreover, large coal pillars must be retained to maintain the stability of the roadway, resulting in a significant loss of coal resources. To solve these dilemmas, gob-side entry retaining (GER), as a modified entry layout using a "Y" type ventilation manner (see Fig. 1(b)), has been widely applied to highly gassy FMCF. In this system, a previous tailgate of the former panel is maintained as a return airway to be reused for the next new panel by constructing an artificial wall along the gob, which can effectively prevent gas accumulation in the upper corner of the coalface and greatly increase coal recovery rate. Also, the application of this retaining technique can significantly decrease roadway driving quantity and shorten the process of mining and tunneling [Liu, Ning, Tan et al. (2018); Yang, Cao, Wang et al. (2016)].

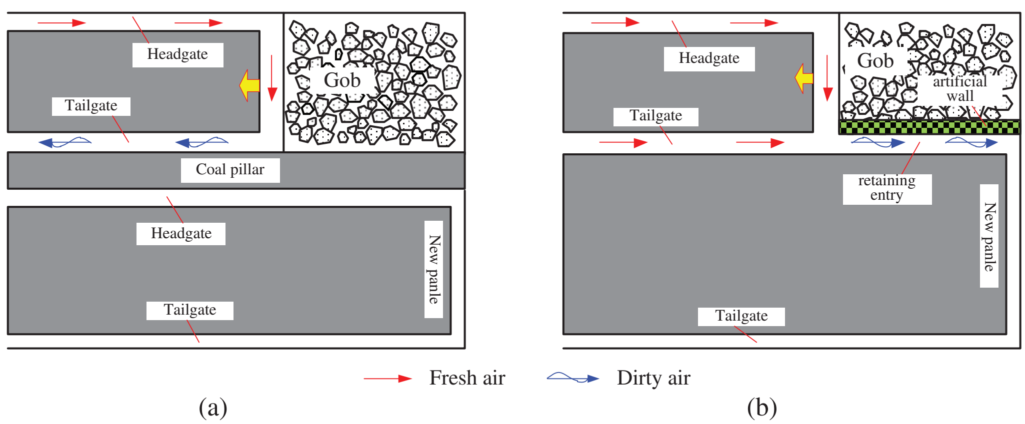

Figure 1: Entry layouts of different longwall mining system: (a) U type longwall mining system; (b) Y type longwall mining system

To date, many researchers have achieved abundant results about the support method, support theory, and filling material of GER technology [Ning, Wang, Bu et al. (2017); Qin, Fu and Chen (2019); Sun, Du, Zhou et al. (2019)]. Concerning the support material, early roadside support materials used include deck wood, dense prop, and concert block, all of which present some defects, such as poor performance to isolate the coalface and gob, high labour intensity, and low construction efficiency [Wang, Wen, Jiang et al. (2018); Yin, Meng, Zhang et al. (2018)]. In recent years, paste material and high water-content material have been widely adopted in a coal mine site because of their high support resistance and improved isolation performance. Concerning the support theory and method, Zhang et al. [Zhang, Yuan, Han et al. (2012)] discussed the roof break law and its structural feature under different immediate roof conditions and derived the theoretical calculation formula for support resistance of a gob-side wall. Tan et al. [Tan, Yu, Ning et al. (2015)] presented a new type of “flexible-hard” combination backfilling body used to counteract the rapid subsidence of the roof. Deng et al. [Deng and Wang (2014)] explored the stress and deformation evolution law of GER in an inclined seam and proposed the corresponding reinforcing method. However, previous studies [Kang, Niu, Zhang et al. (2010); Ma, Gong, Fan et al. (2011); Xu, Chen and Bai (2016)] concerning the stability control of the gob-side entry retaining mainly focused on adjusting the width of the filling wall or increasing the supporting strength, and the GER techniques for thin and medium-thick coal strata are mature. While for the conditions of large mining height and thick-hard main roof, many accidents (such as roof collapse and wall instability) can easily occur due to the overburden loading and abrupt movement of the lateral roof strata [Yin, Jing, Su et al. (2018); Wang, Li, Li et al. (2019)]. In fact, during the movement of the lateral roof, the coal seam wall, the gob-side wall, and the caved rocks in the gob jointly undertake the overburden loading as a whole support system [Wang and Li (2017); Yang, Cao and Li (2011)]. The failure of any one of these bearing structures will result in the failure of the GER [Ning, Liu, Tan et al. (2018)]. Researches showed the bearing capacities of the caved rocks increased exponentially with the strain, while the bearing capacities and allowable deformations of the coal seam wall and backfilling body were limited. The coal wall should increase the support density, and the backfilling body should be of greater width and high strength to endure the significant rotation and deformation of the lateral roof, such requirements will significantly increase the support cost and construction period. By increasing the height of the caved rocks rationally, the movement space of the lateral roof can be significantly reduced, and most of the overlying load can be transferred to the caved rocks. This approach could an effective means to control the stability of GER-FMCF.

In this paper, to effectively control the rotation of lateral roof strata, pre-split blasting technology was proposed to cut down the lower main roof and convert it into the caved rocks, which can effectively reduce the movement space of the lateral roof strata. Firstly, a compatible deformation model was established to reveal the coordinated deformation relationship among the bearing structures. Second, the instability estimate method for the bearing structures was proposed. Then, the optimal roof cutting height was obtained based on the compatible deformation model. Furthermore, the GER-FMCF models with varying roof-cutting heights were simulated with the Universal Distinct Element Code (UDEC) software and the correctness of theoretical analysis is verified. Lastly, field tests in the Tangan coal mine, Ltd., Shanxi Province, China, was conducted to verify the practicability of the design method.

2 Compatible deformation rationale

2.1 Compress deformation model

Substantive theoretical research studies and engineering practices [Ju and Xu (2013); Zha, Shi, Liu et al. (2017)] had proved the overlying strata movement process and broken structure form of GER-FMCF, as shown in Fig. 2. With the advancement of the coal face, the immediate roof caved firstly when the maximum tensile stress reached its limited strength, and then fracture lines I, II, III, and IV formed successively in the main roof. Consequently, the main roof fractured in the shape of "O-X" and a lateral cantilever structure (key block B) would be formed along the gob edge [Qian, Miao and He (1994)]. Because of its massive weight and extensive loading from the overlying strata, the key block B would rotate and sink until it compacted the caved rocks in the gob, as illustrated in Fig. 2(b). In this period, the coal seam wall, the gob-side wall, and the caved rocks commonly undertook the load from the main roof and immediate roof to maintain the stability of gob-side entry retaining. Hou et al. [Hou and Li (2001)] proposed the concept of "big and small structure" in GER-FMCF. The

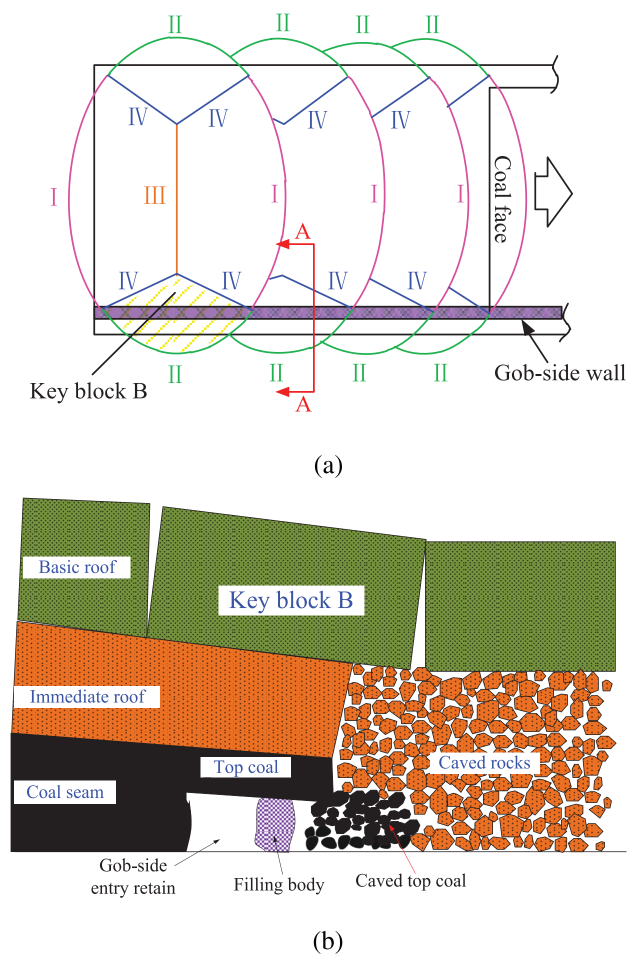

Figure 2: Roof fracture evolution process for GER-FLTC: (a) Plan map of gob-side entry retaining; (b) A-A section view

key curved triangular block B, as the "big structure", exerted significant influence on the stability of the "small structure". Li et al. [Li, Ju, Yao et al. (2016)] suggested that the fracture location, rotation and sagging of lateral cantilever structure played a crucial role in stabilizing the underlying load-bearing structure.

The rotation and subsidence of the key block B were irreversible and irresistible. Thus, the bearing structures should possess larger deformability to bear the given deformation due to the rotation of the lateral roof cantilever rotation [Li, Li, Fan et al. (2015); Hu, Ma, Guo et al. (2018)]. Considering the stiffness of the roof strata is much larger than that of the coal seam and the backfilling body, the compaction deformation of the roof strata can be ignored during the rotation of the key block B. The subsidence of the key block B above the coal seam wall, h_1, can be regarded as the compaction deformation of coal seam wall, and the subsidence of key block B above the gob-side wall can be regarded as the compaction deformation of the gob-side wall, h_2, which is composed of the deformation of backfilling body and the top coal above it.

Based on the above analysis and the geometric equivalence relation in Fig. 3, the compaction and deformation, h_1 and h_2, respectively, can meet a specific relationship with the subsidence of key block B above the caved rocks in the gob, as shown in Eq. (1).

$$\tan\theta = \frac{h_1}{x_0} = \frac{h_2}{x_0 + x_1 + x_2} = \frac{h_3}{L\cos\theta} \tag{1}$$

where θ is the rotation angle of the key block B (°), x_0 is the horizontal distance from the main roof beam end fracturing to the coal wall (m), x_1 is the width of roadway (m), x_2 is the width of the gob-side wall (m), L is the length of key block B (m) and h_3 is the subsidence of key block B above the caved rocks in the gob (m).

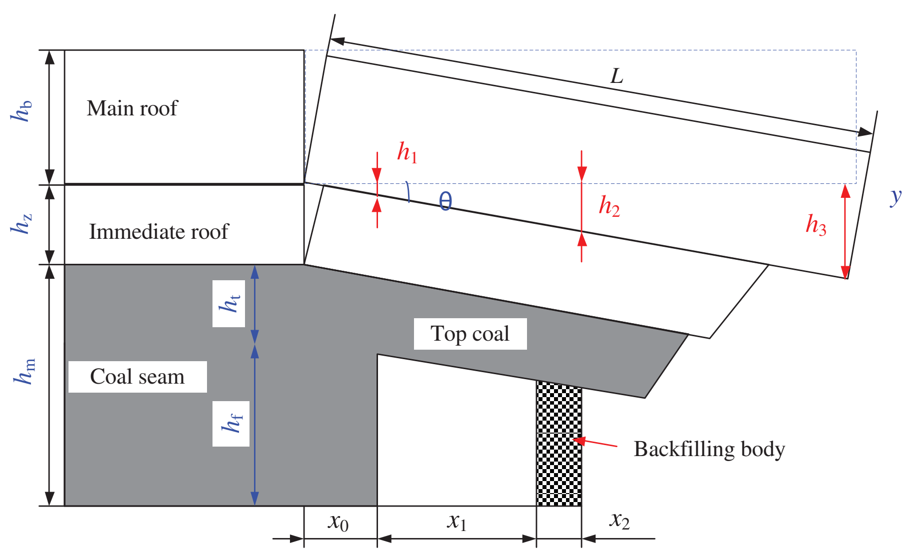

Figure 3: Compatible deformation model for GER-FLAC

Furthermore, under certain engineering geological conditions, the subsidence of key block B above the caved rocks in the gob, h_3, can be obtained by using geometric equivalence relation, as follows:

$$h_3 = h_m + h_z - k_z h_z - k_m h_t \tag{2}$$

where h_m is the thickness of the coal seam, h_z, is the thickness of the immediate roof, k_z is the expansion factor of the caved rocks after compaction, k_m is the expansion factor of the caved coal after compaction and T is the thickness of the top coal.

The compaction deformation, h_1, h_2, is determined by the rotation and sagging of the key block B, the more serious the rotation, the larger the compaction deformation. However, both the coal seam and the backfilling body have an ultimate deformation, once the deformation exceeds their ultimate bearing capability, several roadway instabilities, such as roof caving, backfilling body wall collapsed, will be triggered.

2.2 Compress deformation capacity analysis for coal seam wall

As the rotating pivot point, the coal seam wall would encounter serious stress concentration During the rotation of the main roof. Plastic failure or collapse may occur when the concentrated stress exceeded the ultimate compressive strength σ_{Mmax}. Thus, the deformation of the coal seam wall has a limiting value h_{1max}. For the convenience of analysis and calculation, here, the compress deformation stage was simplified to elastic deformation until the coal seam wall reaches the peak strength. The ultimate compaction deformation of coal seam wall can be calculated as:

$$h_{1\max} = \frac{h_m \sigma_{M\max}}{E_m} \tag{3}$$

where σ_{Mmax} is the uniaxial compressive strength of coal seam wall (MPa) and E_m is the elasticity modulus of the coal seam wall (GPa).

2.3 Compress deformation capacity analysis for gob-side wall

The deformation stage of the top coal and backfilling body were also simplified to elastic deformation. Based on the analysis of the compatible deformation model in Fig. 1(c), h_2 is composed of the deformation of the backfilling body and the top coal. To ensure the successful implementation of the gob-side entry retaining, the bearing load should not exceed the ultimate compressive strength of either the top coal or the filling body. Hence, the ultimate compress compaction of the gob-side wall can be derived as follows:

$$h_{2\max} = \min\{\sigma_{M\max}, \sigma_{f\max}\} \cdot \left(\frac{h_t}{E_m} + \frac{h_f}{E_f}\right) \tag{4}$$

where σ_{fmax} is the ultimate compressive strength of the backfilling body, E_f is the elasticity modulus of the backfilling body, h_f is the height of the backfilling body.

3 Instability estimate method and control measures

The key block B plays a critical role in stability control of the gob-side entry retaining, and excessive rotational deformation may lead to instability for the coal seam wall or the gob-side wall. Thus, presplitting blasting methods were adopted to cut down the lower main roof and convert it into caved rocks. The approach could effectively reduce the movement space of key block B and restrain its rotation extent. The optimal roof cutting height could be determined according to the deformability of the coal seam wall and gob-side wall.

3.1 Stability control for coal seam wall

The approximate relationship curve of h_1, h_3, and the key block B rotation angle (θ) was obtained according to Eq. (1), as shown in Fig. 4.

The deformation value nonlinearly increased with the increase of rotation angle θ, and there was an ultimate deformation value $h_{1\max}$ for the coal seam wall at point a, which determined the rotation angle θ should be less than θ_1. In other words, once θ was larger than θ_1, the compress deformation of the coal seam wall would exceed its ultimate deformation, resulting in collapse or instability accidents.

In a specific engineering situation, h_3 could be obtained by Eq. (2). Therefore, the corresponding compaction deformation for coal seam wall, h_1, should be calculated as:

$$h_1 = \frac{x_0}{L\cos\theta} h_3 \tag{5}$$

Moreover, the ultimate compaction deformation for the coal seam wall (point a in Fig. 4), $h_{1\max}$, could be derived according to the method described in Section 2.1. The condition

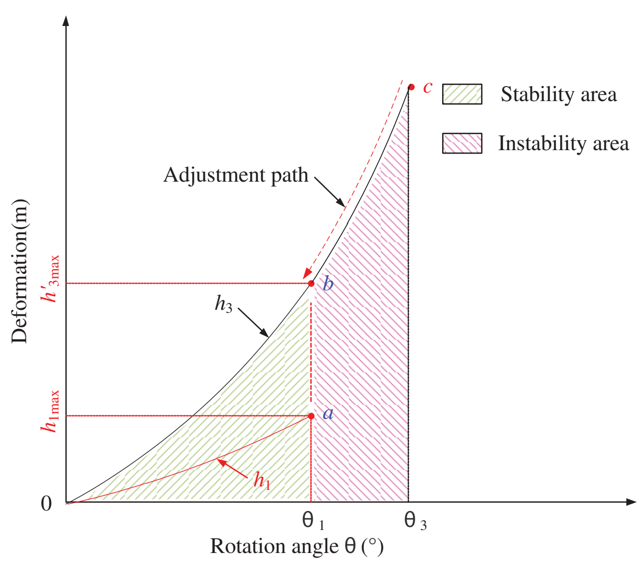

Figure 4: Adjustment diagram for the coal seam wall instability

needed to guarantee the stability of the coal seam wall is,

$$\frac{x_0}{L\cos\theta}h_3 \leq \frac{h_{\mathrm{m}}\sigma_{\mathrm{M\,max}}}{E_{\mathrm{m}}} \tag{6}$$

If $h_1 < h_{1\max}$, the given compaction deformation of the coal seam wall did not exceed its ultimate deformation capacity, and the coal seam wall remained safe and stable. The next task was to verify the deformation capacity of the gob-side wall.

However, if $h_1 > h_{1\max}$, the coal seam was prone to instability because of the excessive rotation of key block B. The maximum allowable subsidence of key block B above caved rocks (point b in Fig. 4), $h'_{3\max}$, can also be calculated as:

$$h'_{3\,\max} = \frac{h_{1\,\max}L\cos\theta}{x_0} \tag{7}$$

Thus, measures should be taken to decrease the subsidence of key block B from point c to point b, as shown in Fig. 4. The roof cutting method could effectively reduce the movement space in the gob, and the minimum thickness of roof strata, h_{c}', which should be cut down, was calculated as:

$$h_{\mathrm{c}}' = \frac{h_{\mathrm{m}} - k_{\mathrm{m}}T - h'_{3\,\max}}{k_z - 1} \tag{8}$$

3.2 Stability control for gob-side wall

Fig. 5 shows that the ultimate compaction deformation ($h_{2\max}$) for the gob-side wall is at point a, which can be calculated by Eq. (4). Once the given compaction deformation of the gob-side wall caused by the rotation of the key block B exceeded the ultimate deformation, collapse or crushing may occur.

Similarly, the irresistible subsidence of key block B above the caved rocks, h_3, was obtained by Eq. (2). Thus, the corresponding compaction deformation of the gob-side wall, h_2, was calculated as:

$$h_2 = \frac{x_0 + x_1 + x_2}{L\cos\theta}h_3 \tag{9}$$

Therefore, the following requirements should be met for the gob-side wall to be stable:

$$\frac{x_0 + x_1 + x_2}{L\cos\theta}h_3 \leq \min\{\sigma_{\mathrm{M\,max}}, \sigma_{\mathrm{f\,max}}\} \cdot \left(\frac{h_{\mathrm{t}}}{E_{\mathrm{m}}} + \frac{h_f}{E_{\mathrm{f}}}\right) \tag{10}$$

If $h_2 < h_{2\max}$, the given compress deformation of the gob-side wall caused by the rotation of key block B was acceptable.

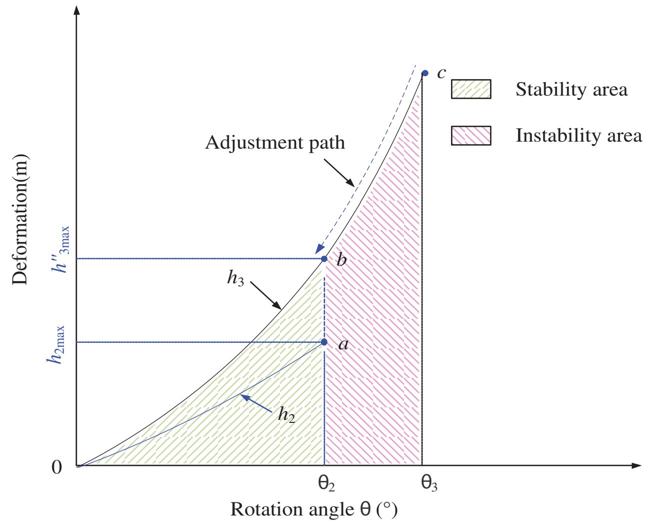

Figure 5: Adjustment diagram for the gob-side wall instability

In contrast, if $h_2>h_{2max}$, the stability of the gob-side wall was potentially threatened, and measures should be taken to limit the rotation of key block B. The maximum allowable subsidence of key block B (point b in Fig. 5), h''_{3max}, was obtained as:

$$h''_{3\,max}=\frac{h_{2\,max}L\cos\theta}{x_0+x_1+x_2} \tag{11}$$

The theoretically required roof cutting height can be easily derived as follows:

$$h_c''=\frac{h_m-k_mT-h''_{3\,max}}{k_z-1} \tag{12}$$

Based on theoretical research and field tests, it could be concluded that the higher the roof-cutting height, the easier it was to maintain the gob-side entry retaining. Thus, the final determined roof-cutting height should be the bigger one between h_c' and h_c''.

4 Determination of roof-cutting parameters

4.1 Geological conditions

A typical field test was conducted at the No. 3307 working face in Tangan Mine, Ltd., Shanxi Province, China. The average mining depth is 350 m, and the mineable coal seam has a mean thickness of 6.25 m and an average dip angle of 5.5°. The geological structure of this coal seam is simple. The immediate roof is formed by mudstone, sandy mudstone and siltstone with an average thickness of 9.2 m. Above the immediate roof is the thick-hard main roof with a thickness of 20.1 m, which is composed of medium-fine sandstone and fine sandstone. Detailed lithological descriptions of the rock strata are illustrated in Tab. 1.

Table 1: Stratigraphic description of the 3307 coal face

Remarks	Name	Thickness (m)	Symbol	Lithology characterization
Overlying strata	Sandy mudstone	8.6		Light gray, muddy structure containing plant fossils
Main roof	Medium-fine sandstone	7.4		Grey to grey white, siliceous cementation, hard
	Fine sandstone	12.7		Gray to dark gray, layered structure, hard and compact
Immediate roof	Sandy mudstone, Mudstone	9.2		Light gray, muddy structure containing plant fossils
	3#coal stratum	6.25		Black, shiny glass, endogenetic fissure development
Immediate floor	Mudstone	5.4		Gray, muddy cementation, and crisp

After the No. 3307 working face was mined out, the backfilling body made of height-water material was installed in the inner roadway side. The width of the retained entry is 4.4 m, and the backfilling body is 3.2 m in height and 1.4 m in width.

4.2 Theoretical analysis of the roof-cutting design

The required parameters to calculate the rotation and settlement of the key block B mainly include: the thickness of the coal seam, 6.25 m, the thickness of immediate roof, h_z=9.2 m, the thickness of main roof, h_b=20.1 m, the roadway width, x_1=4.4 m, the backfilling body width, x_2=1.4 m, and the length of key block B, L, 15.6 m, which was nearly equal to the periodic weighting of the main roof [Li, Hua and Cai (2012)]. The horizontal distance from the key block B end-fracturing to the coal wall, x_0, was estimated as 2.2 m according to a theoretical derivation [Hou and Ma (1989)]. Moreover, the expansion factor of the caved rocks after compaction, k_z, could be set as 1.15.

Substituting the above parameters into Eqs. (1) and (2), the corresponding compaction deformation of the coal seam wall and gob-side wall, h_1 and h_2, were calculated as 0.18 m and 0.64 m, respectively.

To obtain the mechanical parameters of the coal seam wall and the gob-side wall, we first carried out laboratory tests of rock mechanics on the coal samples and the backfill body specimen. Fig. 6 shows the test process and results. The peak strength for coal samples and backfilling body specimen were 16.2 MPa and 12.3 MPa, respectively. The corresponding elastic moduli for the coal samples and the backfilling body specimen were 1.1 GPa and 0.72 GPa, respectively.

However, the rock mass is the synthesis of intact rocks and fissures, and differences exist between the mechanical parameters of intact rock and rock masses. According to the research results of previous studies [Singh and Rao (2005); Zhang and Einstein (2004)], the mechanical parameters of the coal seam and backfilling body can be approximately calculated by follows:

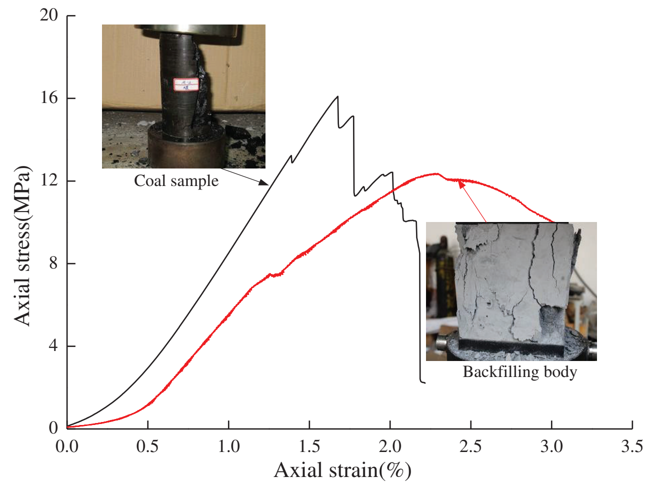

Figure 6: Uniaxial compressive strength test

$$E_{mass} = E_r \cdot 10^{0.0186RQD - 1.91} \tag{13}$$

$$\sigma_{mass} = \sigma_r \cdot \left[\frac{E_{mass}}{E_r}\right]^n \tag{14}$$

where E_{mass} and E_r are the elastic moduli of intact rock and a rock mass, respectively; σ_{mass} and σ_r are the uniaxial compressive strength of an intact rock and a rock mass, respectively; the RQD values were obtained by using a borehole camera; n was set to 0.63 [Singh and Rao (2005)].

Thus, the peak strength for coal seam and backfilling body, σ_{Mmax} and σ_{fmax}, were calculated as 6.9 MPa, and 6.5 MPa, respectively. Also, the corresponding elastic moduli for the coal mass and backfilling body, E_m and E_f, could be obtained as 0.28 GPa and 0.26 GPa, respectively.

Substituting the above parameters into Eqs. (3) and (4), the maximum allowable compaction deformation of the coal seam wall and the gob-side wall, h_{1max} and h_{2max}, were calculated as 0.27 m and 0.28 m, respectively. The calculated given deformation of the gob-side wall (h_2) is obviously larger than h_{2max}. As a consequence, the gob-side wall would easily collapse or be damaged caused by excessive rotation of the lateral roof.

To effectively limit the rotational deformation of key block B, measures should be taken to increase the height of the caved rocks in the gob. Substituting h_{2max} into Eqs. (11) and (12), the required roof cutting height can be calculated as 17.8 m.

5 Numerical modeling of the GER-FMCF

5.1 Distinct element method

The discrete element method (DEM) is an attractive computational method used by many investigators to study the movement of a large number of particles under given conditions. The DEM was initially developed as a two-dimensional representation of jointed rock masses, but it has also been extended to the application of particle flow studies, micro mechanism studies of granular materials, and the crack development in rock and concrete. In the DEM, a rock material is treated as an assembly of discrete blocks or particles. It simulates the discontinuous discrete elements according to the constitutive relation of between the contacts and Newton's second law between all blocks. Compared with the finite element method (FEM), the DEM possess considerable advantages in simulating the process of roof fracture, movement and large deformation. Thus, in this paper, a distinct element code (UDEC) is adopted to investigate the effect of roof-cutting height on the stability of the retained entry.

The UDEC software is one of the most commonly used two-dimensional distinct element programs. It is mainly used for analysis in rock engineering projects, ranging from studies of the progressive failure of rock slopes to evaluations of the influence of rock joints, faults, bedding planes, etc., on underground excavations and rock foundations [Yang, Chen, Fang et al. (2018); Itasca Consulting Group, Inc. (2008)]. It is also well-suited for studying potential failure modes that are directly related to the presence of discontinuous features. In the Distinct Element Method, the rock mass is regarded as an assemblage of discrete blocks bonded along their joints. The joints between the blocks are treated as the discontinuities, which allow the blocks to move and rotate along the discontinuity surface. Individual blocks act like a rigid or deformable material. The deformable blocks are subdivided into finite-difference elements, and the response of each element conforms to the prescribed linear or nonlinear stress-strain law. The relative motion of the discontinuous is also controlled by linear or non-linear force-displacement relationships that move in the normal and shear directions. The dynamic relaxation algorithm is adopted to solve the systems of equations formed and the development of large displacements is allowed when the failure occurs. Large displacements are straightforward in the UDEC, which are caused by the rigid body motion of individual blocks, including block rotation, fracture opening and complete detachments. Thus, the UDEC has a unique advantage to simulate the fracturing and movement of the rock strata in underground mining.

Duo to the tensile strength of the rock is far less than its compressive strength. The Mohr-Coulomb elastoplastic constitutive model is adopted to realize the tensile failure of the blocks. The failure criterion (σ_1, σ_3) is illustrated in Fig. 7.

The following Mohr-Coulomb yield function was used to failure envelope from point A to point B,

$$f^s=\sigma_1-\sigma_3 N_\varphi+2c\sqrt{N_\varphi} \tag{15}$$

and from point B to C by a tension yield function of the form

$$f^{\mathrm{t}}=\sigma^{\mathrm{t}}-\sigma_3 \tag{16}$$

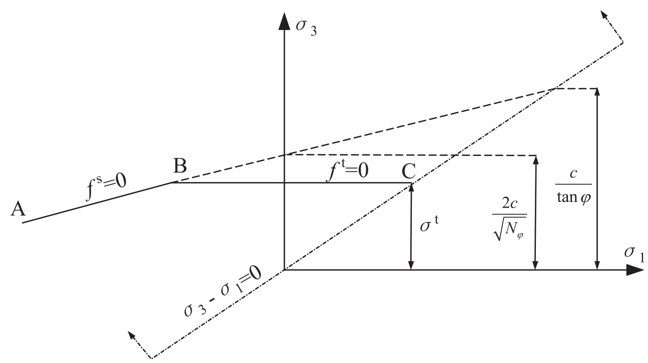

Figure 7: Mohr-Coulomb failure criterion for block in UDEC [Itasca Consulting Group, Inc. (2008)]

where φ is the friction angle, c is the cohesion, N_φ=(1+sinφ)/(1-sinφ), σ^t is the tensile strength.

For the contacts, the Coulomb friction law is applied to simulate the sliding or opening of the contact, which very suitable to simulate the failure process of rock roadway after excavation. Fig. 8 shows the constitutive behavior of the contact.

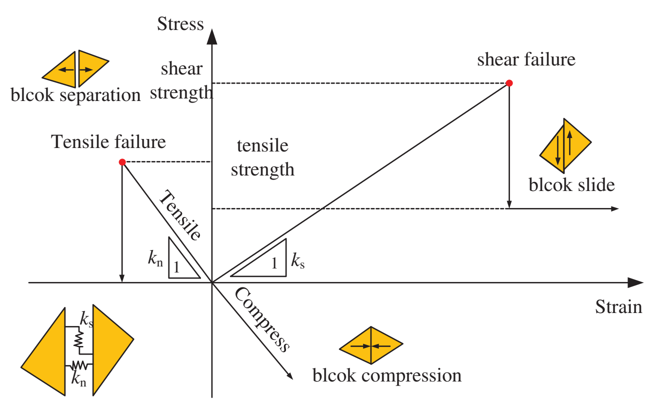

Figure 8: The constitutive behavior of the contact

In the normal direction of the contact, the contact behavior is determined by the normal stiffness k_n, and the force-displacement relation is assumed to be linear.

$$\Delta\sigma_n = -k_n \Delta u_n \tag{17}$$

where $\Delta\sigma_n$ is the valid normal force increment and Δu_n is the normal displacement increment.

Once the normal force exceeds the tensile strength of the contact, then σ_n will turn to be zero, and tensile failure will occur.

In the shear direction of the contact, the contact behavior is governed by the shear stiffness k_s. The shear stress τ_s is limited by several contact micro properties, such as cohesion (C), friction angle (ϕ). Thus, if

$$|\tau_s| \leq C + \sigma_n \tan\phi = \tau_{max} \tag{18}$$

Then

$$|\tau_s| = -k_s \Delta u_s{}^e \tag{19}$$

Or else, if

$$|\tau_s| \geq \tau_{max} \tag{20}$$

Then

$$|\tau_s| = sign(\Delta u_s)\tau_{max} \tag{21}$$

where $\Delta u_s{}^e$, Δu_s are the elastic shear displacement increment and the total shear displacement increment, respectively.

5.2 Calibration of micro-parameters

The mechanical behavior of the rock material is closely related to its micro-properties of the blocks and contacts. Thus, a series of experiments should be carried out to calibrate the micro-parameters before they can be used to model a specific rock [Wu, Liang, Zhou et al. (2020)].

First, a series of laboratory rock mechanics tests were carried out on the intact rock to obtain the original micro-parameters. The mechanical parameters of the rock mass could be obtained by Eqs. (13) and (14). Then the normal and shear stiffness of the contacts, k_n and k_s , were calculated using the following formulas.

$$k_n = 10\left[\frac{K + \frac{3}{4}G}{\Delta z_{min}}\right] \tag{22}$$

$$k_s = 0.4k_n \tag{23}$$

where K and G are the bulk modulus and shear modulus, respectively. Δz_{min} is the smallest width of the zone adjoining the contact in the normal direction [Itasca Consulting Group, Inc. (2008)].

Finally, a large number of uniaxial compression numerical tests were performed iteratively to achieve a good agreement between the numerical simulation and laboratory testing results. The stress-axial strain curves of the numerical simulation tests are shown in

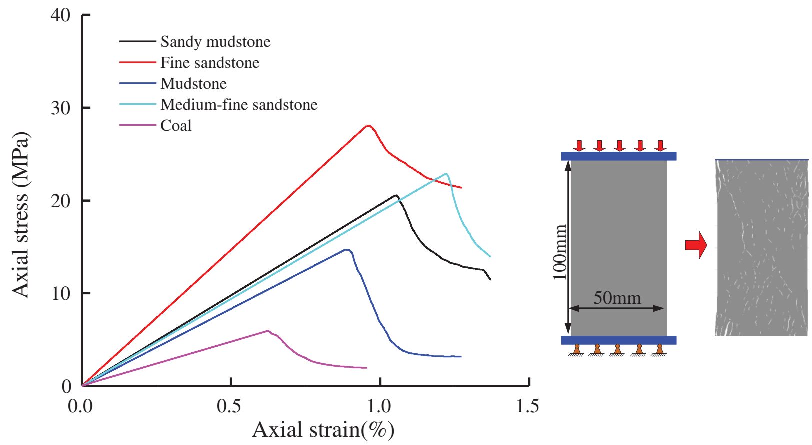

Figure 9: Simulated compression tests and stress-strain curves of the rock mass

Table 2: Physical and mechanical parameters of rock mass used in the UDEC model

Lithology	Block properties			Contact properties				
	Density (kg/m^3)	K (GPa)	G (GPa)	k_n (GPa/m)	k_s (GPa/m)	C_j (MPa)	Φ_j (°)	σ_t^j (MPa)
Sandy mudstone	2030	0.52	0.28	86.2	34.48	1.18	23	0.26
Medium-fine sandstone	2560	1.72	1.05	243.5	97.4	1.64	30	0.32
Fine sandstone	2720	1.84	1.20	264.8	105.92	1.75	32	0.32
Coal	1400	0.65	0.30	68.4	27.36	0.98	22	0.22
Mudstone	1800	0.72	0.35	79.6	31.84	1.12	23	0.24

Fig. 9, and the final calibrated parameters of blocks and contacts used in the UDEC model are summarized in Tab. 2.

5.3 Model establishment

The roof-cutting height plays a vital role in the stability of gob-side entry retaining structures. In order to determine a rational roof-cutting height, numerical models with varying roof-cutting heights were established to investigate the effect of the roof-cutting technique on the retaining entry. The calculated model with a dimension of 120 m in width and 76.2 m in height was established based on the geological conditions of the No. 3307 working face. The retaining roadway was 4.4 m wide and 3.2 m high, and the backfilling body was 1.4 m wide and 3.2 m high. A 25-m-wide region was preserved at the left of the model to avoid the boundary effect. The lateral boundaries were restrained by horizontal displacement, and the bottom boundary was fixed with the vertical displacement. A vertical stress of 7 MPa was applied to the upper boundaries to simulate the overburden stress. Previous studies had proved that the trigon blocks have a significant advantage in cogently describing the failure process of roadway surrounding compared with the rectangular blocks. Thus, for the area of interest around the roadway, the rock masses were divided into trigon blocks, with an average edge length of less than 0.3 m. The remaining regions were divided into rectangular blocks to improve the calculation speed. The detailed simulation model is shown in Fig. 10.

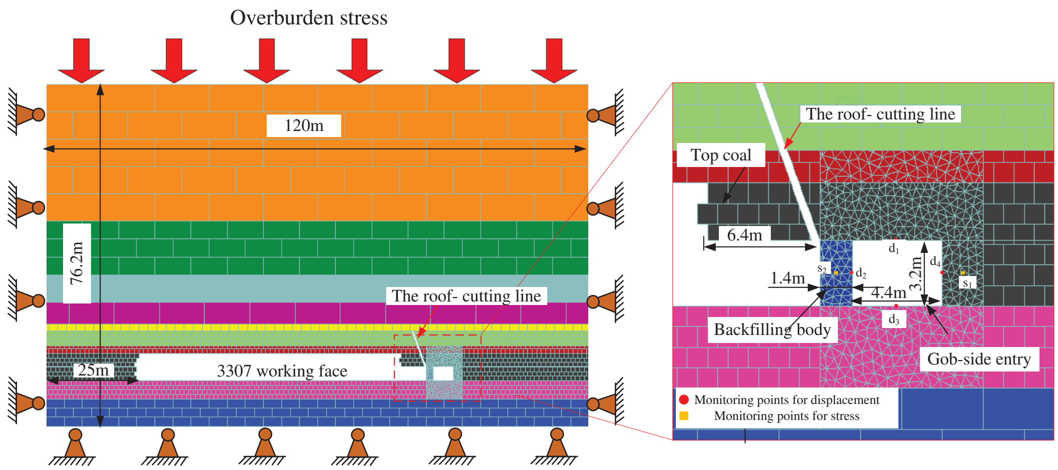

Figure 10: Numerical model for GER-FMCF

Firstly, before the excavation of the roadway and the panel, the numerical model was run into an equilibrium state to form the initial stress. Then, the roadway was excavated by deleting the relevant blocks to simulate the excavation. The excavated roadway would suffer a certain degree of deformation under the action of initial in-situ stress. After the excavated roadway reached a stable state, the predesigned roof-cutting line was constructed by deleting the blocks within its region, and then the No. 3307 working face was excavated. At the same time, the filling wall was built after the excavation of the panel. During the simulation calculation, several monitoring points were set on the surface and inside of the surrounding rock of the roadway, which was aimed to record the change in displacement and stress, as shown in Fig. 10. In this paper, five numerical models with varying roof-cutting height ranging from 6 m to 22 m were created to reveal the stress distribution and deformation pattern of GER-FMCF. The roof-cutting height was defined as the vertical height of the roof-cutting line. In order to better determine the appropriate cutting height, the cutting angle was fixed at 70°.

5.4 Numerical modeling results

5.4.1 Stress evolution analysis

Fig. 11 displays the vertical stress maps of the GER with different roof-cutting height.

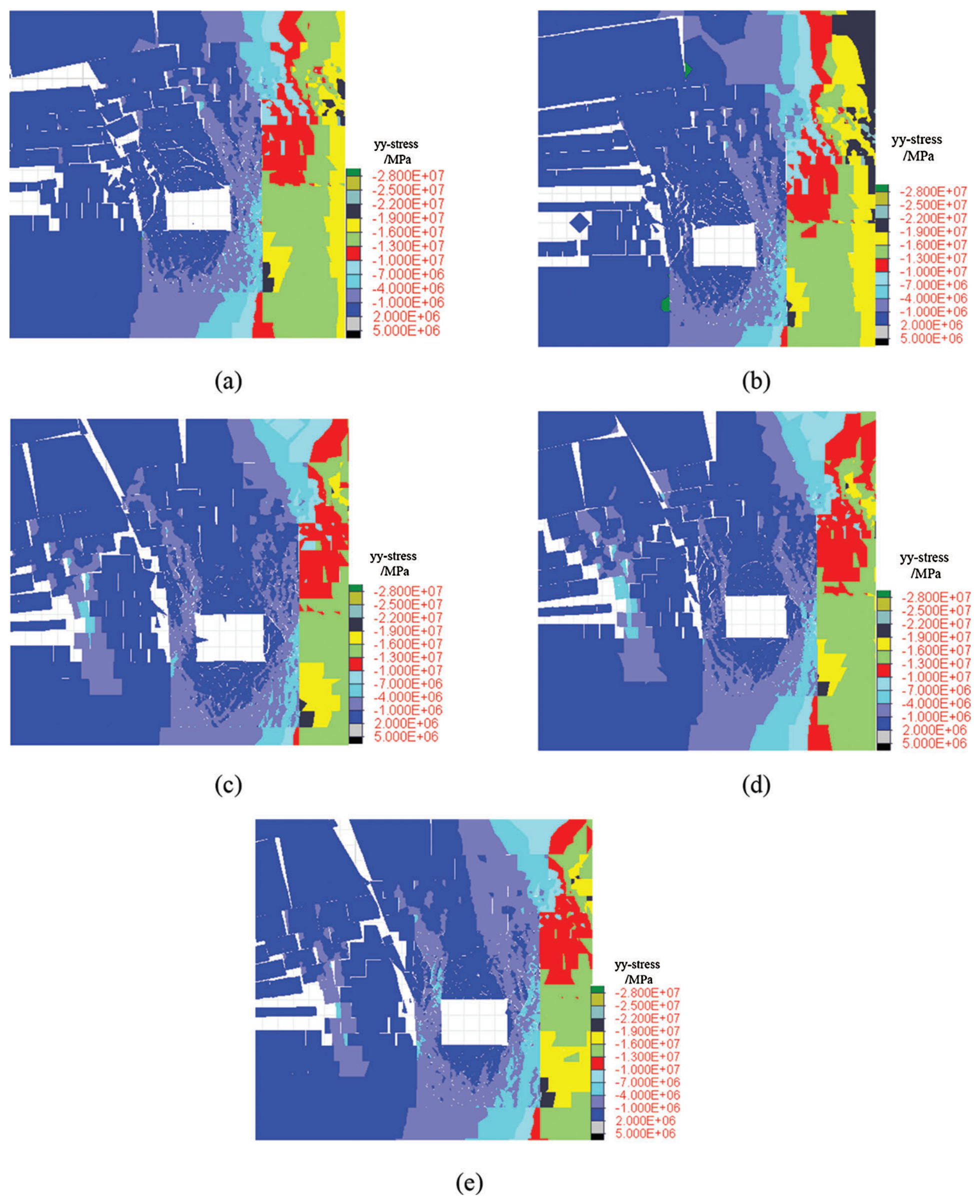

Figure 11: Numerical calculation results of vertical stress distributions for different roof-cutting height: (a) 6 m; (b) 10 m; (c) 14 m; (d) 18 m; (e) 22 m

For the condition of 6 m roof-cutting height (Fig. 11(a)), the immediate roof strata could not cave timely to fill the gob, leaving larger rotation space for the main roof strata. Thus, the bearing structures of GER, including the backfilling body and the coal seam wall would bear the enormous load from the overlying strata, which resulted in a significant stress concentration. The peak of the vertical stress for the backfilling body and coal seam wall was 17.8 MPa and 23.2 MPa, respectively. In this situation, the coal or backfill would be destroyed, resulting in un-stability of the GER. As the roof-cutting height increases to 10 m (Fig. 11(b)), the cantilever structure of the immediate roof was easy to be cut off, and the peak stress of the backfilling body and the coal seam wall decreased to 15.6 MPa and 20.5 MPa, with a reduction rate of 12.3% and 11.4%, respectively. However, there was still a more significant stress concentration due to the movement of the main roof. When the roof-cutting height was 14 m (Fig. 11(c)), the stress environment of GER was improved to some extent, where the peak stress of the backfilling body and the coal seam wall decreased by 35.3% and 18.9%, decreased to 11.5 MPa and 18.8 MPa, respectively. It was because that part of the main roof strata had been cut down and converted into the caved gangue, which restrained the rotation and subsidence of the overlying main roof. As the roof-cutting height further increased to 18 m (Fig. 11(d)), the main roof was completely cut off, and the load transmitted by the overlying strata was greatly eliminated. The peak stress of the backfilling body and the coal seam wall decreased to 9.6 MPa and 16.7 MPa, with a reduction rate of 46% and 28%, respectively. In this condition, the GER-FMCF could be successfully implemented. When the roof-cutting height increased to 22 m (Fig. 11(e)), the peak stress of the backfilling body and the coal seam wall was 10.2 MPa and 17.5 MPa, which was similar to that of 18-m-roof-cutting height. It could conclude that the stress environment of the gob side entry cannot be further improved when the cutting height exceeds 18 m.

5.4.2 Displacement analysis

Figs. 12 and 13 present the final vertical and horizontal displacement nephogram of the GER with different roof-cutting height, respectively. The deformation of surrounding rock in GER was greatly affected by the roof-cutting height. When the roof-cutting height was less than 10 m, the GER would encounter severe deformation, and many large cracks appeared in both the coal seam wall and backfilling body. The coal seam wall and backfilling body were easy to be destroyed by the irresistible rotation and subsidence of the overlying strata, resulting in the failure of GER. When the roof-cutting height increased to 14 m, the rotation and sinking of the main roof were limited to some extent, and the caved rocks would share more loading from the overlying strata in the gob. All of these made the deformation of GER can be controlled effectively. The convergence between roof and floor and that between the two sides was about 260 mm and 184 mm, respectively, as shown in Figs. 12(c) and 13(c). As the roof-cutting height increased to 18 m, the deformation of the surrounding rock of GER further decreased. The maximum convergence between roof and floor was about 196 mm, while the maximum convergence of the two sides was about 82 mm. When the cutting height reached 22 m, the deformation state of the surrounding rock was similar to the condition of 18-m-roof-cutting height. The deformation of the roadway surroundings was reduced obviously as the increase of the roof-cutting height.

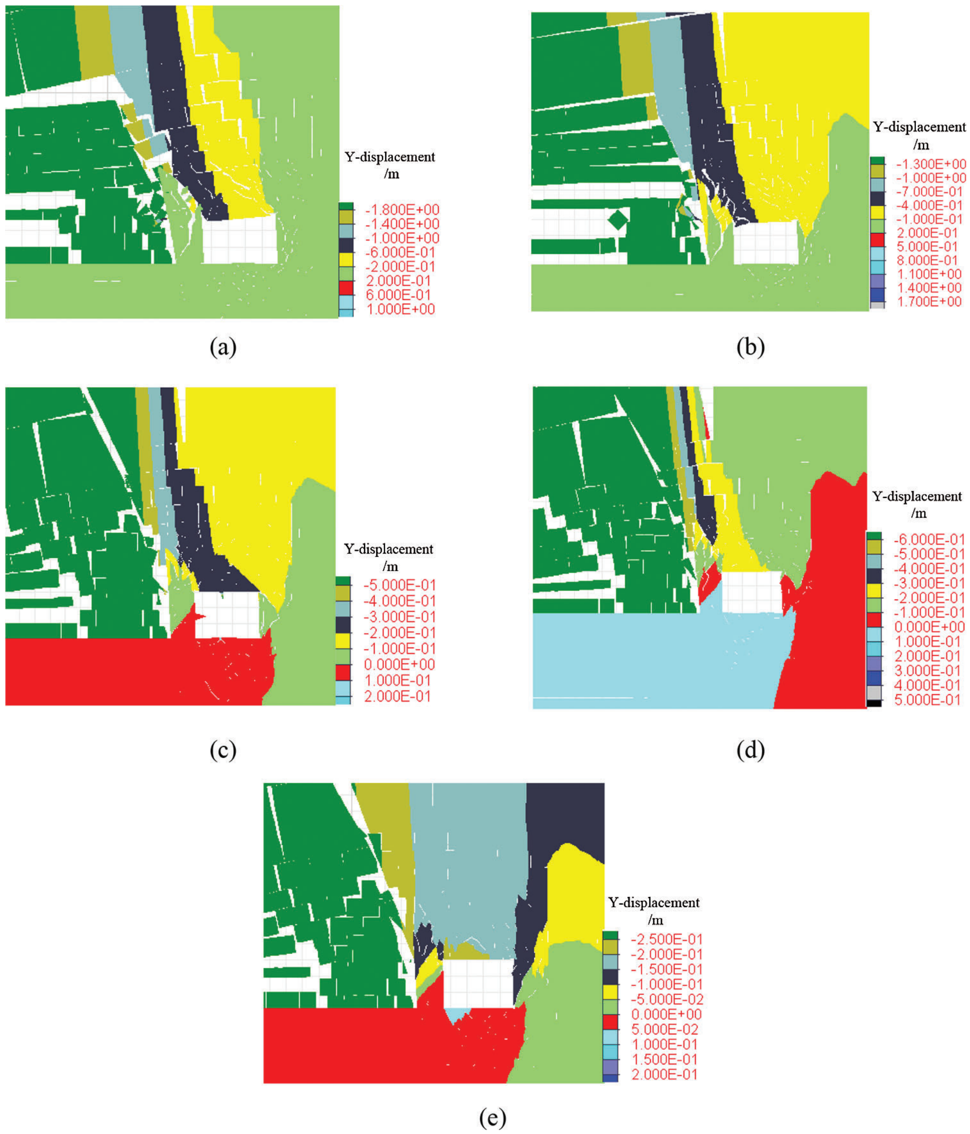

Figure 12: Vertical displacement nephogram of GER with different roof-cutting height: (a) 6 m; (b) 10 m; (c) 14 m; (d) 18 m; (e) 22 m

In order to accurately and quantitatively compare and analyze the surrounding rock deformation of GER with different cutting heights, four monitoring lines were set along the roof and floor and two sides of the entry to record displacement variation. The monitoring results are presented in Fig. 14.

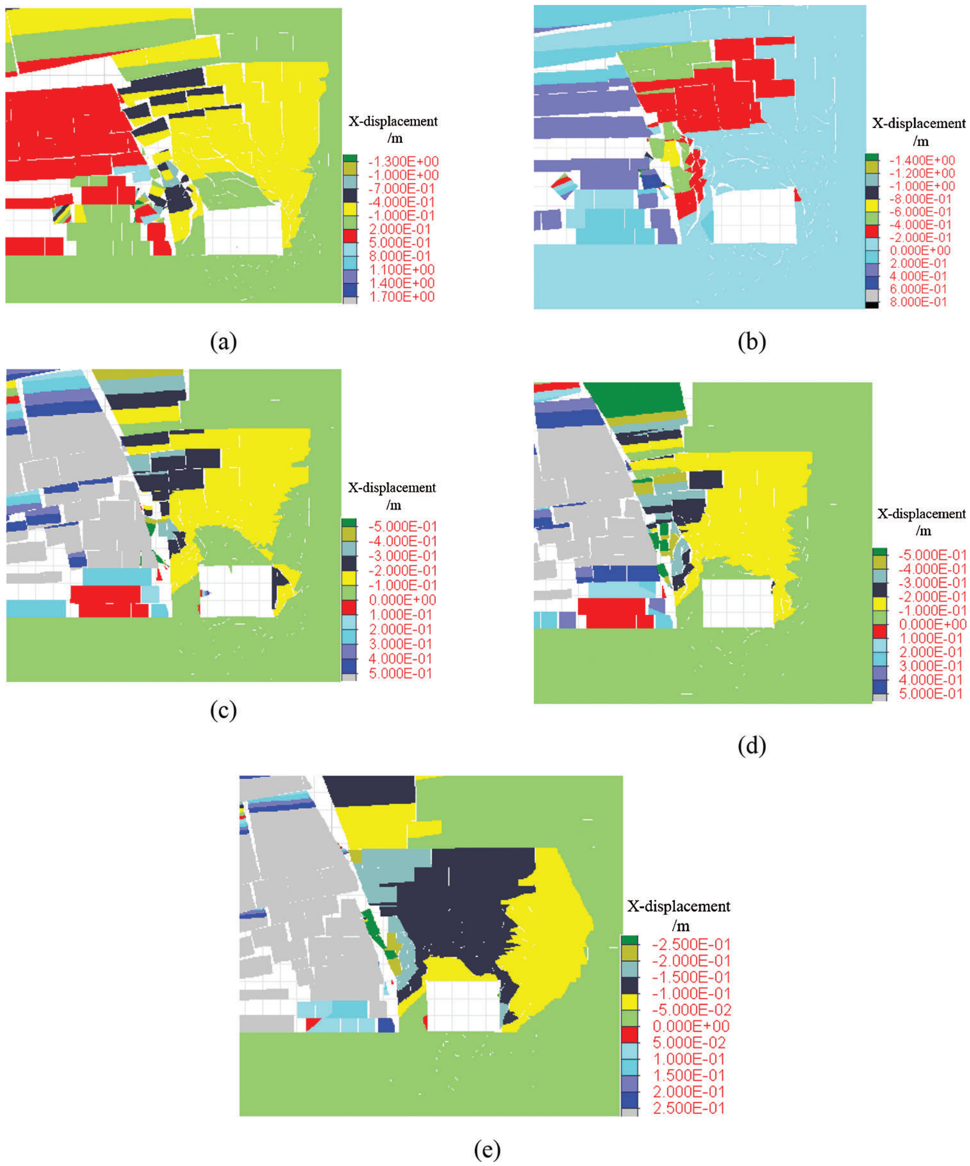

Figure 13: Horizontal displacement nephogram of GER with different roof-cutting height: (a) 6 m; (b) 10 m; (c) 14 m; (d) 18 m; (e) 22 m

The horizontal deformation of the backfilling body was significantly affected by the roof-cutting height, and the maximum deformation usually occurred in its upper part. At 6 m roof-cutting height, the maximum horizontal displacement of the filling body was about 272 mm. As the roof-cutting height increased to 10 m, the maximum horizontal displacement decreased to 240 mm, with a reduction rate of 11.7%. As the roof-cutting

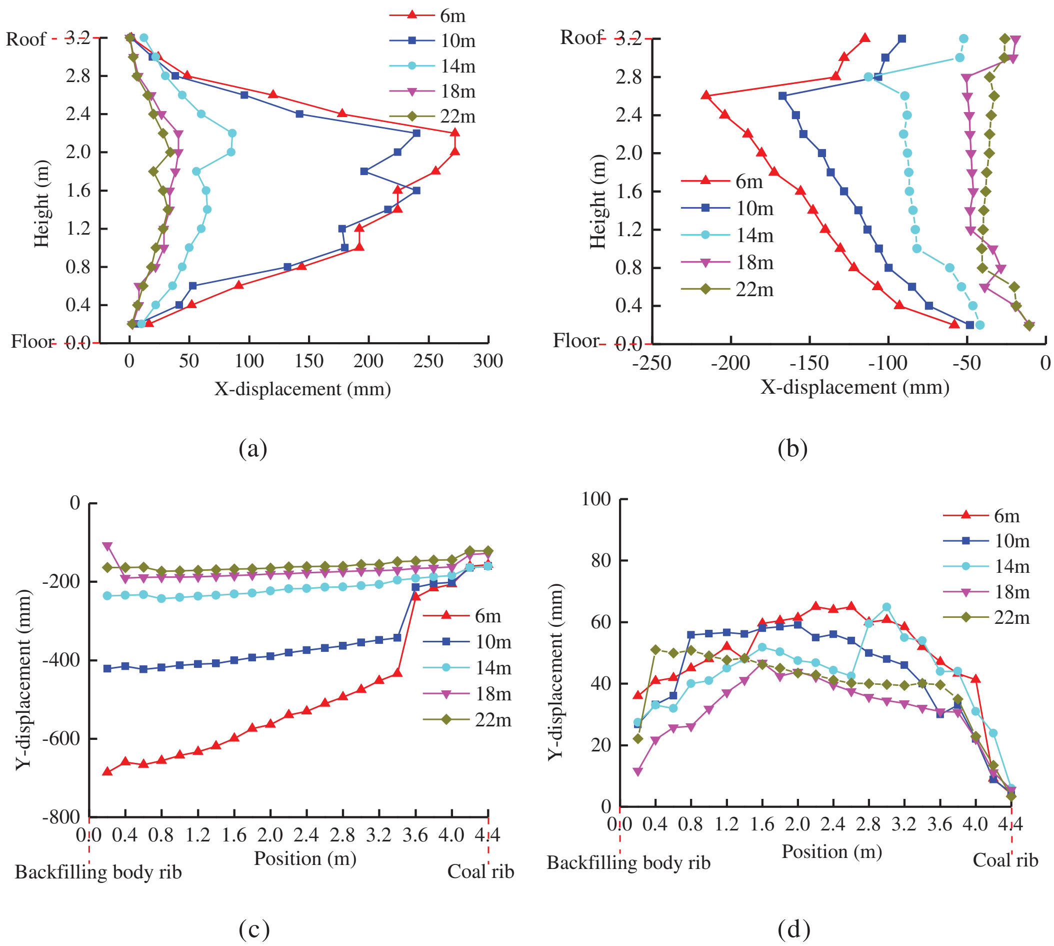

Figure 14: Displacement of the surrounding rock of GER with different roof-cutting height: (a) X-displacement of the backfilling body rib; (b) X-displacement of the coal rib; (c) Y-displacement of the roof; (d) Y-displacement of the floor

height increased to 14 m, the maximum horizontal displacement decreased by 66.9% with 182 mm decrement. When the cutting height continued to increase to 18 m, the maximum horizontal displacement reduced to 40.8 mm, with a reduction rate of 85%. When the cutting height was 22 m, the maximum horizontal displacement was about 34 mm, which was similar to that of 18-m-roof-cutting height.

A similar changing trend could be observed for the coal rib, as shown in Fig. 14(b). The maximum horizontal deformation of the coal rib also occurred in its upper part, which may attribute to the rotation and sinking of the main roof. At 6 m roof-cutting height, the maximum horizontal displacement was about 215 mm. As the roof-cutting height increased to 10 m, the maximum deformation decreased to 167 mm, with a reduction rate of 22.3%. At 14 m roof-cutting height, the deformation of the coal rib was further controlled, decreased to 90 mm, with a reduction rate of 58.1%. As the cutting height increased to 18 m, the maximum horizontal displacement severely decreased by 76.7% with a 125 mm decrement. As the cutting height increased to 22 m, the maximum deformation decreased to 40 mm.

Fig. 14(c) displays the vertical displacement of the roof for different roof-cutting height. The roof-cutting height also had a significant influence on the sagging of the roof. The roof sagging adjacent to the backfilling wall is more significant than that adjacent to the coal seam wall, which is especially apparent when the cutting height was at 6 and 10 m. When the roof-cutting height was 6 m, the maximum subsidence of the roof was about 686 mm. As the cutting height increased to 10 m, the roof subsidence decreased to 423 mm, with a reduction rate of 38.3%. As the cutting height increased to 14 m, the maximum subsidence reduced by 64.7% with a 440 mm decrement. As the cutting height continued to increase to 18 m, the roof subsidence further decreased, and the maximum subsidence was only about 188 mm, which could meet with mine production requirements well. As the cutting height further increased to 22 m, the roof subsidence changed little compared with that of 18-m-roof-cutting height, and the maximum subsidence was about 173 mm.

Compared with the roof subsidence, the floor heave was little affected by the roof-cutting height, as shown in Fig. 14(d). When the cutting height was 6 and 10 m, the maximum floor heave was about 64 mm and 61 mm, respectively. As the cutting height increased to 18 and 22 m, the floor heave was slightly changed, decreased to 45 mm and 48 mm, respectively.

Based on the above numerical simulation results analysis, we can conclude that roof-cutting height has a significant effect on the stability of the surrounding rock of GER. The deformation of the GER can be effectively controlled when the roof-cutting height exceeded to 18 m. The numerical simulation results verified the theoretical analysis well.

6 Field application

6.1 Presplitting blast scheme

Presplitting blasting technology was implemented in the roof to cut down the lower main roof strata and convert it into caved rocks in the gob, aiming to limit the rotation space of the key block B [Wang, Tu, Yuan et al. (2013)]. The blast holes were constructed ahead of the working face by 20 m. The blast hole depth was approximately 18 m, with a horizontal angle of 70°. The spacing between the two blast holes was approximately 2.5 m, and the borehole diameter was 75 mm. The sealing length and the charging length were 8 m and 11 m, respectively. Simultaneously, an additional empty hole was drilled between the two blast holes, which could increase the fracture penetration rate and utilization rate of the explosive energy. The detailed borehole arrangements parameters are shown in Fig. 15.

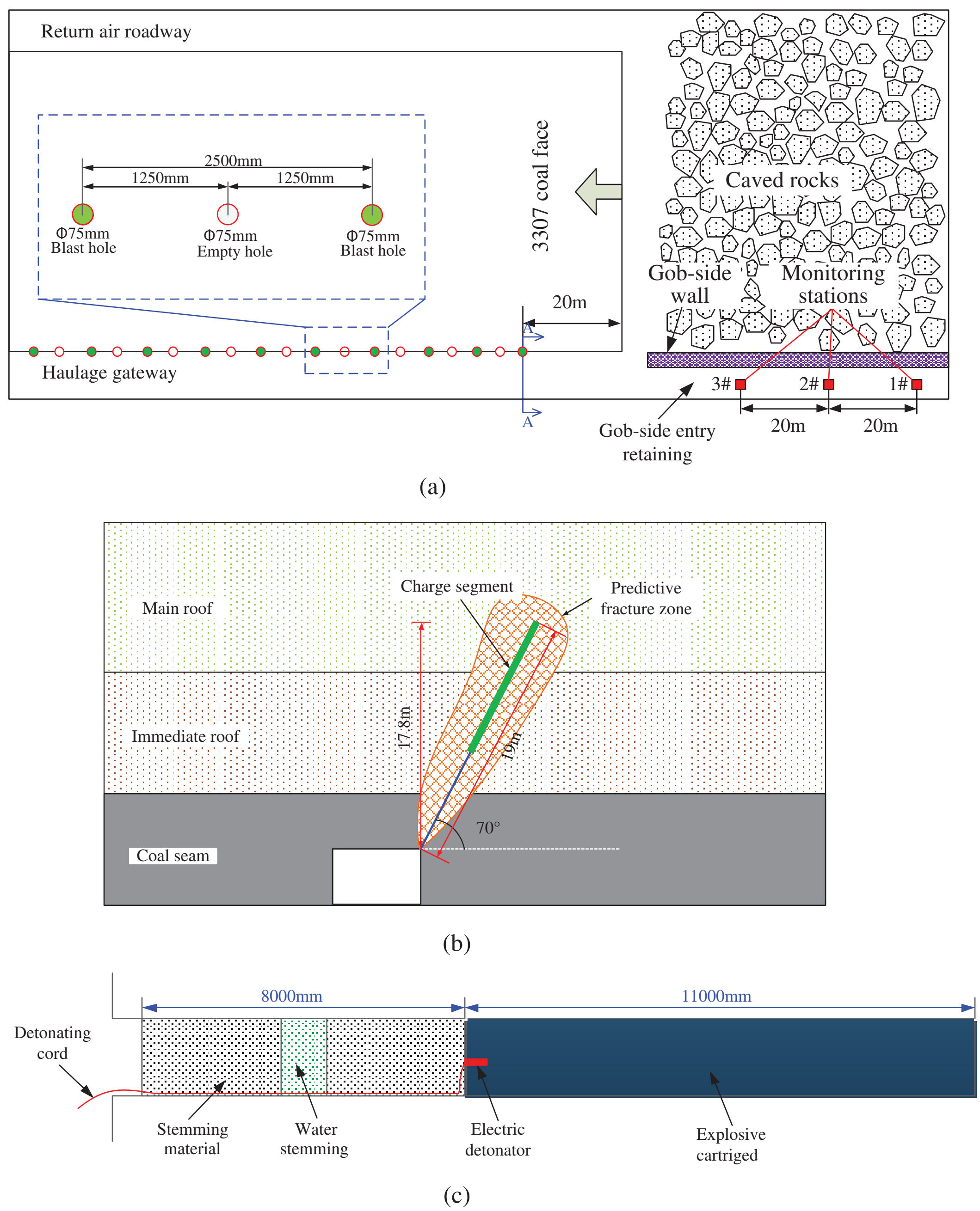

Figure 15: The layout of drilling holes: (a) Plan view; (b) A-A section view; (c) Charge structure of blast hole

6.2 Effect analysis

To analyze the effects of the presplitting blast on the surrounding rocks of GER, three monitoring stations were set up along the No. 3307 haulage gateway (red solid rectangle in Fig. 15(a)). The distance between adjacent monitoring stations was 20 m. Each station contains supporting force monitoring for the gob-side wall via borehole stress-meters and surrounding rock deformation monitoring via cross-point measurement (see Fig. 16(a)). Displacement meters were installed to record the roof-to-floor convergence (see Fig. 16(b)).

Fig. 17 shows the monitoring results of the deformation of retaining entry and supporting force of the backfilling body. The deformation of retaining entry relatively small. The

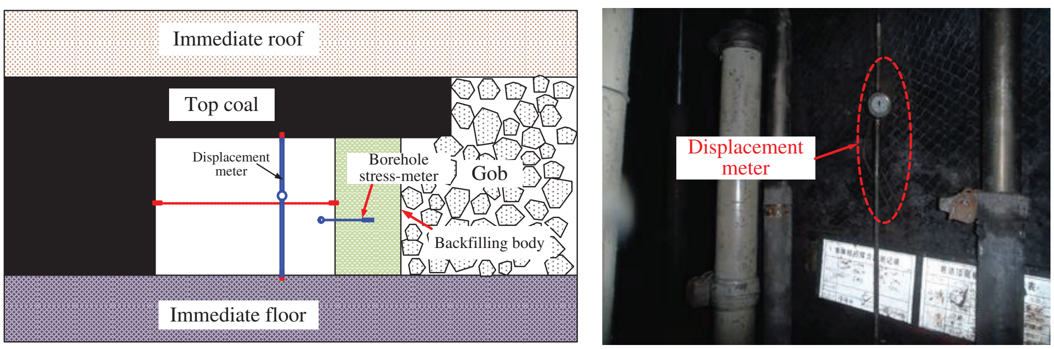

(a) (b)

Figure 16: Monitoring schematic diagram

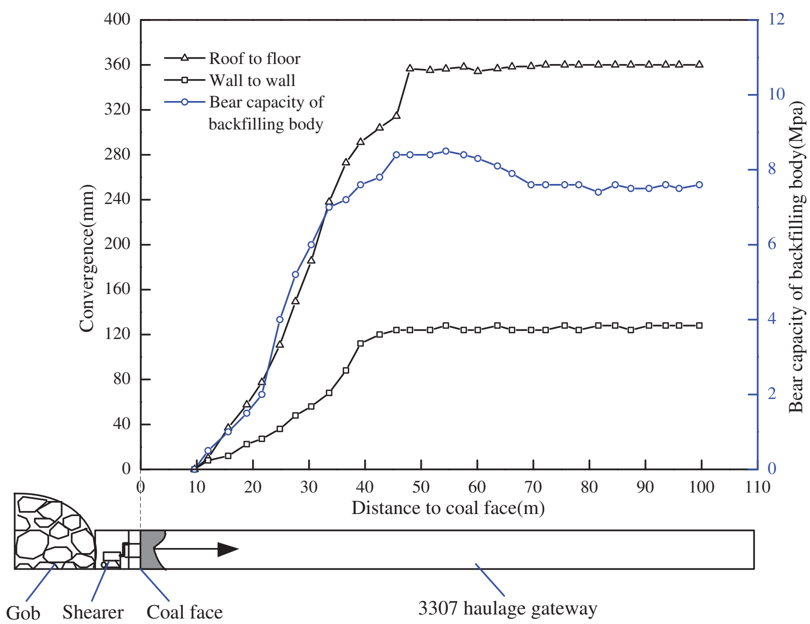

Figure 17: Filed monitoring results

largest convergence of the roof to floor and wall to wall were 361 mm and 122 mm, respectively. As the coalface passed the monitoring station at a distance of 40 m, the supporting force of the gob-side wall reached a maximum value of 8.5 MPa, and then began to reduce and was almost stabilized at around 7.5 MPa. The control effect of gob-side entry retaining in the coal mine site was shown in Fig. 18. Field monitoring results indicated that the deformation of GER-FMCF can be effectively controlled by roof cutting technology, and the optimal roof cutting height obtained by theoretical derivation was reasonable.

(a) (b)

Figure 18: Photograph of gob-side entry retaining

7 Conclusions

This study aimed to obtain a rational roof cutting height to ensure the stability of GER-FMCF. The design flows mainly include the following four steps: (1) Establishing the compatible deformation model for GER-FMCF. (2) Obtaining the ultimate deformability of the coal seam wall and gob-side wall. (3) Estimating the bearing capacity of the coal seam wall and the gob-side wall according to the instability judgment. (4) Determining the optimal roof-cutting height using Eqs. (8) and (12).

To verify the accuracy of theoretical deduction, numerical models of GER-FMCF with different roof-cutting height were established according to the background of No. 3307 haulage gateway in the Tangan coal mine. The numerical simulation results showed that the deformation of the roadway was severe and the backfilling body and coal rib were easily to fail when the cutting height is less than 18 m. As the cutting height increased to 18 m, the stress environment of the roadway was much improved, and the deformation of the surrounding rock could be effectively controlled. The numerical simulation results could verify the conclusion of theoretical deduction well.

Finally, engineering verification was conducted in the No. 3307 haulage gateway in the Tangan coal mine, Ltd., Shanxi Province, China. According to the theoretical deduction and numerical simulation result, the cutting height was set as 18 m. Presplitting blasting technology was implemented in the roof strata with a roof cutting angle of 70°. The maximum convergence between roof and floor was about 361 mm, and the maximum convergence of the two sides was about 122 mm. The monitoring results proved that the deformation of the surrounding rock of GER-FMCF could be effectively controlled.

Note that this research was mainly focused on the compatible deformation mechanism of the load-bearing structures (coal seam wall, gob-side wall and caved rocks). In the process of theoretical deduction, some assumptions and idealizations were applied to simplify the calculations. Further studies, such as the bearing capacity of bolted coal and backfilling body in the field site, must be conducted to optimize the availability of the model.

Acknowledgement: The authors would like to thank the Editor and the anonymous reviewers for their helpful and constructive comments.

Funding Statement: This work is financially supported by National Natural Science Foundation of China (Nos. 51734009, 51904290), the Natural Science Foundation of Jiangsu Province, China (BK20180663).

Conflicts of Interest: The authors declare that they have no conflicts of interest to report regarding the present study.

References

Deng, Y. H.; Wang, S. (2014): Feasibility analysis of gob-side entry retaining on a working face in a steep coal seam. *International Journal of Mining Science and Technology*, vol. 24, no. 4, pp. 499-503. DOI 10.1016/j.ijmst.2014.05.013.

Hou, C. J.; Li, X. H. (2001): Stability principle of big and small structures of rock surrounding roadway driven along goaf in fully mechanized top coal caving face. *Journal of China Coal Society*, vol. 26, no. 1, pp. 1-7.

Hou, C. J.; Ma, N. J. (1989): Stress in in-seam roadway sides and limit equilibrium zone. *Journal of China Coal Society*, vol. 4, pp. 21-29.

Hu, S. X.; Ma, L. Q.; Guo, J. S.; Yu, P. J. (2018): Support-surrounding rock relationship and top-coal movement laws in large dip angle fully-mechanized caving face. *International Journal of Mining Science and Technology*, vol. 28, no. 3, pp. 533-539. DOI 10.1016/j.ijmst.2017.10.001.

Itasca Consulting Group, Inc. (2008): *UDEC User Manual*. Minneapolis, MN, USA: Itasca Consulting Group, Inc..

Ju, J. F.; Xu, J. (2013): Structural characteristics of key strata and strata behaviour of a fully mechanized longwall face with 7.0 m height chocks. *International Journal of Rock Mechanics and Mining Sciences*, vol. 58, no. 1, pp. 46-54. DOI 10.1016/j.ijrmms.2012.09.006.

Kang, H. P.; Niu, D.; Zhang, Z.; Lin, J.; Li, Z. et al. (2010): Deformation characteristics of surrounding rock and supporting technology of gob-side entry retaining in deep coal mine. *Chinese Journal of Rock Mechanics & Engineering*, vol. 29, no. 1, pp. 1977-1987.

Li, A.; Liu, Y.; Dai, F.; Liu, K.; Wei, M. (2020): Continuum analysis of the structurally controlled displacements for large-scale underground caverns in bedded rock masses. *Tunnelling and Underground Space Technology*, vol. 97.

Li, S.; Li, J. W.; Fan, C. J.; Luo, M. K.; Han, Y. L. (2015): Roof subsidence laws and control technology for gob-side entry retaining in fully-mechanized top coal caving face. *Journal of China Coal Society*, vol. 40, no. 9, pp. 1989-1994.

Li, X. H.; Ju, M.; Yao, Q.; Zhou, J.; Chong, Z. (2016): Numerical investigation of the effect of the location of critical rock block fracture on crack evolution in a gob-side filling wall. *Rock Mechanics and Rock Engineering*, vol. 49, no. 3, pp. 1041-1058. DOI 10.1007/s00603-015-0783-1.

Li, Y. F.; Hua, X. Z.; Cai, R. C. (2012): Mechanics analysis on the stability of key block in the gob-side entry retaining and engineering application. *Journal of Mining & Safety Engineering*, vol. 29, no. 3, pp. 357-364.

Liu, X. S.; Ning, J. G.; Tan, Y. L.; Gu, Q. H. (2018): Coordinated supporting method of gob-side entry retaining in coal mines and a case study with hard roof. *Geomechanics and Engineering*, vol. 15, no. 6, pp. 1173-1182.

Ma, Z. G.; Gong, P.; Fan, J.; Geng, M.; Zhang, G. (2011): Coupling mechanism of roof and supporting wall in gob-side entry retaining in fully-mechanized mining with gangue backfilling. *Mining Science and Technology (China)*, vol. 21, no. 3, pp. 829-833. DOI 10.1016/j.mstc.2011.05.036.

Ning, J. G.; Wang, J.; Bu, T. T.; Hu, S. C.; Liu, X. S. (2017): An innovative support structure for gob-side entry retention in steep coal seam mining. *Minerals*, vol. 7, pp. 775.

Ning, J. G.; Liu, X. S.; Tan, J.; Gu, Q. H.; Tan, Y. L. et al. (2018): Control mechanisms and design for a 'coal-backfill-gangue' support system for coal mine gob-side entry retaining. *International Journal of Oil, Gas and Coal Technology*, vol. 19, no. 3/4, pp. 444. DOI 10.1504/IJOGCT.2018.093132.

Qian, M. G.; Miao, X. X.; He, F. L. (1994): Analysis of key block in the structure of voussoir beam in longwall mining. *Journal of China Coal Society*, vol. 31, no. 32, pp. 191A.

Qin, Z.; Fu, H. L.; Chen, X. X. (2019): A study on altered granite meso-damage mechanisms due to water invasion-water loss cycles. *Environmental Earth Sciences*, vol. 78, no. 14, pp. 428. DOI 10.1007/s12665-019-8426-6.

Singh, M.; Rao, K. S. (2005): Empirical methods to estimate the strength of jointed rock masses. *Engineering Geology*, vol. 77, no. 1-2, pp. 127-137. DOI 10.1016/j.enggeo.2004.09.001.

Sun, W. B.; Du, H. Q.; Zhou, F.; Shao, J. L. (2019): Experimental study of crack propagation of rock-like specimens containing conjugate fractures. *Geomechanics and Engineering*, vol. 17, no. 4, pp. 323-331.

Tan, Y. L.; Yu, F. H.; Ning, J. G.; Zhao, T. B. (2015): Design and construction of entry retaining wall along a gob side under hard roof stratum. *International Journal of Rock Mechanics and Mining Sciences*, vol. 77, pp. 115-121. DOI 10.1016/j.ijrmms.2015.03.025.

Wang, F. T.; Tu, S. H.; Yuan, Y.; Feng, Y.; Chen, F. et al. (2013): Deep-hole pre-split blasting mechanism and its application for controlled roof caving in shallow depth seams. *International Journal of Rock Mechanics and Mining Sciences*, vol. 64, pp. 112-121. DOI 10.1016/j.ijrmms.2013.08.026.

Wang, J.; Li, S. C.; Li, L. P.; Lin, P.; Xu, Z. H. et al. (2019): Attribute recognition model for risk assessment of water inrush. *Bulletin of Engineering Geology and the Environment*, vol. 78, no. 2, pp. 1057-1071. DOI 10.1007/s10064-017-1159-4.

Wang, J.; Li, Y. (2017): 12-thick seam coal mining and its ground control. *Advances in Coal Mine Ground Control*, pp. 379-407.

Wang, J.; Yang, S.; Li, Y.; Wei, L.; Liu, H. (2014): Caving mechanisms of loose top-coal in longwall top-coal caving mining method. *International Journal of Rock Mechanics and Mining Sciences*, vol. 77, pp. 160-170. DOI 10.1016/j.ijrmms.2014.04.024.

Wang, J.; Ning, J. G.; Jiang, L. S.; Jiang, J. Q.; Bu, T. T. (2018): Structural characteristics of strata overlying of a fully mechanized longwall face: a case study. *Journal of the Southern African Institute of Mining and Metallurgy*, vol. 118, pp. 1195-1204.

Wang, X.; Wen, Z. J.; Jiang, Y. J.; Huang, H. (2018): Experimental study on mechanical and acoustic emission characteristics of rock-like material under non-uniformly distributed loads. *Rock Mechanics and Rock Engineering*, vol. 15, no. 3, pp. 729-745. DOI 10.1007/s00603-017-1363-3.

Wu, N.; Liang, Z. Z.; Zhou, J. R.; Zhang, L. Z. (2020): Energy evolution characteristics of coal specimens with preformed holes under uniaxial compression. *Geomechanics and Engineering*, vol. 20, no. 1, pp. 55-66.

Xu, Y.; Chen, J.; Bai, J. B. (2016): Control of floor heaves with steel pile in gob-side entry retaining. *International Journal of Mining Science and Technology*, vol. 26, no. 3, pp. 527-534. DOI 10.1016/j.ijmst.2016.02.024.

Yang, H.; Cao, S.; Wang, S.; Fan, Y.; Wang, S. et al. (2016): Adaptation assessment of gob-side entry retaining based on geological factors. *Engineering Geology*, vol. 209, pp. 143-151. DOI 10.1016/j.enggeo.2016.05.016.

Yang, S. L.; Cao, G. M.; Li, F. S. (2011): Underground pressure appearance laws analysis for fully mechanized top coal slice caving on high-dipping thick coal seams. *Journal of Coal Science & Engineering*, vol. 17, no. 1, pp. 6-11. DOI 10.1007/s12404-011-0102-8.

Yang, S. Q.; Chen, M.; Fang, G.; Wang, Y. C.; Meng, B. et al. (2018): Physical experiment and numerical modelling of tunnel excavation in slanted upper-soft and lower-hard strata. *Tunnelling and Underground Space Technology*, vol. 82, pp. 248-264. DOI 10.1016/j.tust.2018.08.049.

Yin, D. W.; Meng, X. X.; Zhang, Z. Y.; Liu, B. (2018): Gob-side entry retaining formed by roof cutting without roadside support. *International Journal of Oil, Gas and Coal Technology*, vol. 18, no. 3/4, pp. 467-484. DOI 10.1504/IJOGCT.2018.093137.

Yin, Q.; Jing, H. W.; Su, H. J.; Zhao, H. H. (2018): Experimental study on mechanical properties and anchorage performances of rock mass in the fault fracture zone.

International Journal of Geomechanics, vol. 18, no. 7, pp. 04018067. DOI 10.1061/(ASCE) GM.1943-5622.0001187.

Zha, W. H.; Shi, H.; Liu, S.; Kang, C. (2017): Surrounding rock control of gob-side entry driving with narrow coal pillar and roadway side sealing technology in Yangliu coal mine. *International Journal of Mining Science and Technology*, vol. 27, no. 5, pp. 819-823. DOI 10.1016/j.ijmst.2017.07.023.

Zhang, L.; Einstein, H. H. (2004): Using RQD to estimate the deformation modulus of rock masses. *International Journal of Rock Mechanics & Mining Sciences*, vol. 41, no. 2, pp. 337-341. DOI 10.1016/S1365-1609(03)00100-X.

Zhang, N.; Yuan, L.; Han, C.; Xue, J.; Kan, J. G. (2012): Stability and deformation of surrounding rock in pillarless gob-side entry retaining. *Safety Science*, vol. 50, no. 4, pp. 593-599. DOI 10.1016/j.ssci.2011.09.010.

Zhang, Z. Z.; Bai, J. B.; Chen, Y.; Yan, S. (2015): An innovative approach for gob-side entry retaining in highly gassy fully-mechanized longwall top-coal caving. *International Journal of Rock Mechanics and Mining Sciences*, vol. 80, pp. 1-11. DOI 10.1016/j. ijrmms.2015.09.001.